

Cluster Expansion Framework for the $\text{Sr}(\text{Ti}_{1-x}\text{Fe}_x)\text{O}_{3-x/2}$ ($0 < x < 1$) Mixed Ionic Electronic Conductor: Properties Based on Realistic Configurations

Bin Ouyang,[†] Tanmoy Chakraborty,[‡] Namhoon Kim,[§] Nicola H. Perry,^{||,⊥} Tim Mueller,[#] Narayana R. Aluru,^{†,‡,§,⊥} and Elif Ertekin^{*,†,§,⊥}

[†]National Center for Supercomputing Applications, University of Illinois at Urbana–Champaign, 1205 W Clark Street, Urbana, Illinois 61801, United States

[‡]Beckman Institute for Advanced Science and Technology, University of Illinois at Urbana–Champaign, 405 N Mathews Avenue, Urbana, Illinois 61801, United States

[§]Department of Mechanical Science and Engineering, University of Illinois at Urbana–Champaign, 1206 W Green Street, Urbana, Illinois 61801, United States

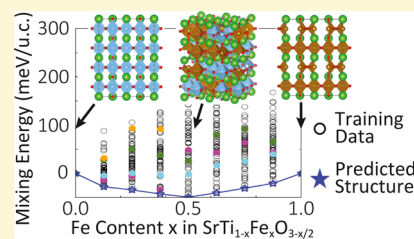
^{||}Department of Materials Science and Engineering and Materials Research Laboratory, University of Illinois at Urbana–Champaign, 1304 W Green Street, Urbana, Illinois 61801, United States

[⊥]International Institute for Carbon Neutral Energy Research (WPI-I2CNER), Kyushu University, 744 Motooka, Nishi-ku, Fukuoka 819-0395, Japan

[#]Department of Materials Science and Engineering, Johns Hopkins University, 3400 N Charles Street, Baltimore, Maryland 21218, United States

Supporting Information

ABSTRACT: Several mixed ionic/electronic conductors (MIECs) used as fuel or electrolysis cell electrodes may be thought of as solid solutions of perovskite oxides and ordered oxygen vacancy compounds. For example, the model MIEC $\text{SrTi}_{1-x}\text{Fe}_x\text{O}_{3-x/2+\delta}$ (STF) can be described as a mixture of the perovskite SrTiO_3 and the brownmillerite $\text{Sr}_2\text{Fe}_2\text{O}_5$ that can accommodate some degree of oxygen off-stoichiometry δ . The large configurational space for these nondilute, disordered mixtures has hindered atomic scale modeling, limiting in-depth understanding and predictive analysis. We present a cluster expansion framework to describe the energetics of the disordered STF system within the full solid solution composition space $\text{Sr}(\text{Ti}_{1-x}\text{Fe}_x)\text{O}_{3-x/2}$, $0 < x < 1$, $\delta = 0$. Cluster expansion Monte Carlo (CEMC) simulations are performed to identify low-energy configurations and to investigate the origin and degree of lattice disorder. Using realistic configurations obtained from CEMC, the electronic structure, band gap, and optical properties of STF and their sensitivity to the stoichiometry are examined and compared to those of hypothetical ordered structures and special quasirandom structures. The predicted evolution of the band gap and optical absorption with composition is consistent with the experiment. Analysis of the electronic structure elucidates that electronic transport within the mixture benefits from the simultaneous presence of Fe/Ti disorder on the B cation sublattice and a tendency for oxygen vacancies to cluster around Fe atoms. The modeling framework adopted here for the $\text{SrTiO}_3/\text{Sr}_2\text{Fe}_2\text{O}_5$ mixture can be extended to other MIEC materials.



1. INTRODUCTION

Mixed ionic electronic conductors (MIECs) exhibiting large electron and oxygen-ion conductivity are important across a variety of solid-state electrochemical devices, including solid oxide fuel and electrolysis electrodes, oxygen separation membranes, oxygen sensors, and catalysts.^{1–7} The $\text{SrTi}_{1-x}\text{Fe}_x\text{O}_{3-y}$ (STF) mixture^{8,9} is a classic example of a MIEC.^{8–15} At high $T > 800$ °C, the STF composition space forms a continuous solid solution between $0 < x < 1$ that, depending on the Ti/Fe composition and thermodynamic environment, exhibits large, tunable ionic and electronic conductivity.^{8,9} This makes the STF solid solution important for several emerging technologies, especially if control over

properties can be achieved by tuning composition, oxygen richness/deficiency, and atomic configurations.

The difficulty in identifying realistic atomic-scale configurations of the nondilute, disordered solution makes it challenging to understand the electronic structure and transport properties of STF. A unified picture of the structure/property relations is still missing, which precludes mechanistic understanding and predictive modeling. The goal of this work is to introduce a computational framework that

Received: October 9, 2018

Revised: April 9, 2019

Published: April 10, 2019

correlates composition, atomic configurations, electronic structure, and optical properties. We present an approach to predict realistic atomic-scale configurations across the full composition space $0 < x < 1$ based on a cluster expansion¹⁶ model. The cluster coefficients are fitted to density functional theory (DFT) calculations to describe the configurational energetics, and the resulting model is used to establish in detail the effects of composition and structure on the electronic and optical properties.

In contrast to previous studies in which dilute Fe-doped SrTiO₃ is used as a reference to understand STF,^{17–21} we adopt a formalism where STF is considered as a continuous solid solution for $0 < x < 1$ between end members SrTiO₃ (perovskite) and Sr₂Fe₂O₅ (brownmillerite).⁸ Although SrTiO₃ is a typical perovskite wide band gap semiconductor,^{22,23} Sr₂Fe₂O₅, itself a MIEC, is a spin-polarized ordered oxygen vacancy compound that undergoes an order/disorder transition at $T = 800$ °C to a disordered, oxygen-deficient perovskite phase.^{2,4,25} We consider compositions SrTi_{1–x}Fe_xO_{3–x/2+δ} with $\delta = 0$ (referred to as the reference composition), as illustrated in Figure 1. Our prior work²⁶

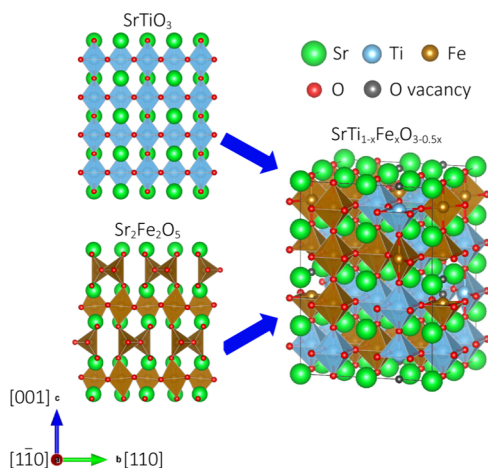


Figure 1. Illustration of the atomic configuration of SrTiO₃, Sr₂Fe₂O₅, and SrTi_{1–x}Fe_xO_{3–x/2} lattices. The SrTi_{1–x}Fe_xO_{3–x/2} can be regarded as a mixture of SrTiO₃ and Sr₂Fe₂O₅ with disorder of Fe and Ti cations.

showed that the reference composition $\delta = 0$ is energetically favorable under a wide range of temperatures and oxygen partial pressures and that when STF is used as the oxygen electrode in fuel or electrolysis cells, only slight deviations $\delta > 0$ and $\delta < 0$ are present for oxidizing and reducing conditions, respectively. The reference composition SrTi_{1–x}Fe_xO_{3–x/2} is naturally associated with an inherent partial occupancy of the oxygen sublattice in which $x/2$ of the usual perovskite oxygen sites is vacant. Here, rather than being defects, these vacant sites are thought of as natural, intrinsic components of the mixture. The disordered solid solutions are reported to exhibit a cubic structure in the experiment across a wide range of temperatures and compositions.^{27–30}

The cluster expansion is a computationally efficient way to describe the evolution of properties across this full composition space $0 < x < 1$. Once formulated, it enables rapid prediction of the energies of different configurations of the mixture. Because the energy is based on the clusters of atoms that appear in the configuration alone, it is only necessary to determine the clusters present to determine the

configurational energy. The cluster expansion approach provides, usually at the cost of some loss of accuracy, an efficient approach to determining energies compared to first-principles methods such as DFT which rely on numerical solution of governing quantum mechanical equations. For example, total energies can be determined in seconds rather than hours or days typically required in DFT. Because of its efficiency, it is possible to use the cluster expansion both to search for low-energy configurations in a large phase space and, when combined with Monte Carlo simulations (CEMC, cluster expansion Monte Carlo), to obtain realistic representations of the material at different temperatures accounting for configurational entropy. Both of these are demonstrated here.

This methodology enables characterization of the degree of Ti/Fe disorder on the B-site sublattice and the O/V_O (oxygen ion/oxygen vacancy) disorder on the oxygen sublattice as a function of composition and temperature. Consistent with prior experiments,^{8,31} we do not observe long-range order but find that at low temperature, short-range order can be present. Because electronic structure, optical properties, and transport properties are sensitive to the local structure, we perform Monte Carlo simulations to identify realistic configurations for selected compositions and temperature. The configurations are used to provide insight into the structure/property relations. We predict a band gap evolution with Fe content that agrees with the experiment.⁸ Together with the electronic structure analysis, we find that the large degree of mixing prevalent in the Fe/Ti sublattice together with the tendency for oxygen vacancies to cluster around Fe atoms helps to spatially distribute the valence band states throughout the STF network and avoid the formation of localized band edge states that would be detrimental for hole transport for sufficiently high Fe content. The properties of the CEMC-predicted configurations are shown to vary widely from those that would be exhibited by hypothetical ordered systems, special quasirandom structures (SQSs), and randomly generated structures, demonstrating the value of the cluster expansion approach. This shows that properties such as the band gap, density of states, and electronic states are sensitive to configurations and that a realistic representation of configurations is necessary to achieve a computational predictive capability, thus demonstrating the value of the cluster expansion. Because many MIEC materials may be considered as mixtures of perovskites and ordered oxygen vacancy compounds, our study not only gives detailed insights into the structure and electronic properties of alloyed SrTiO₃/Sr₂Fe₂O₅ compounds but also provides a framework for investigation and discovery of other perovskite oxide solutions for fuel/electrolysis cell applications^{1–6} and other applications where materials exhibiting substantial disorder are used.

2. METHODOLOGY

2.1. First-Principles Calculations. DFT^{32,33} calculations are used to calculate the total energy and electronic structure of different configurations of STF. We use Vienna Ab initio Simulation Package,^{34–36} the Perdew–Burke–Ernzerhof³⁷ (PBE) description of exchange–correlation, and projector augmented-wave pseudopotentials.³⁸ All calculations include spin polarization. As DFT-PBE does not sufficiently accurately describe localized states of transition metals, onsite U interactions are included for the Ti 3d and Fe 3d states. Without this, DFT-PBE predicts a band gap of 1.67 eV for SrTiO₃ (3.25 eV in the experiment^{2,4,10,22,39}) and a metallic

state for $\text{Sr}_2\text{Fe}_2\text{O}_5$ (2.35 eV gap in the experiment^{8,40}). The parameter U is calibrated by screening all combinations from $U = 0$ eV to $U = 8$ eV for both Ti and Fe and comparing the electronic structure to both experiment and hybrid functional HSE06 calculations. We found that $U = 3$ eV for Ti and $U = 5$ eV for Fe provide a reasonable description of both band gaps (2.13 eV for SrTiO_3 and 0.95 eV for $\text{Sr}_2\text{Fe}_2\text{O}_5$), density of states, and atomic magnetic moments.²⁶ Although DFT + U represents a compromise between accuracy and computational efficiency, it is necessary when simulating a large number of supercells spanning across different compositions and configurations.

To initialize configurations, 160 atom supercells of SrTiO_3 are first constructed and then random substitution of the desired concentration of Ti atoms by Fe atoms and corresponding random removal of O atoms are carried out. Referenced to the traditional perovskite cubic cell, the supercells have lattice vectors oriented along the [110], [110], and [001] direction which makes the supercell also commensurate with the brownmillerite structure. Supercell lattice vector relaxations are permitted in our analysis. Therefore, as illustrated in Figure 1, this supercell can simultaneously capture the structural features of both the cubic SrTiO_3 and the distorted $\text{Sr}_2\text{Fe}_2\text{O}_5$ lattice. For example, as the iron content increases toward $x = 1$ and the vacancy concentration toward $y = x/2 = 0.5$, the vacancies are able to order on the oxygen sublattice and the lattice vectors become distorted in such a way that the brownmillerite structure emerges.

Our analysis is limited to the fixed composition space $\text{SrTi}_{1-x}\text{Fe}_x\text{O}_{3-y}$ with $0 \leq x \leq 1$, $y = x/2$. This amounts to a smooth transition between SrTiO_3 and $\text{Sr}_2\text{Fe}_2\text{O}_5$ and represents the limiting case of fully ionic compensation (i.e., using formal charges, the removal of 1 O^{2-} atom for every 2 Ti^{4+} that are replaced with 2 Fe^{3+} allows the system to remain neutral). This ionic compensation model for STF was suggested earlier⁸ and is commonly referred to as the “reference composition” for the STF solution. It has been experimentally assessed using thermogravimetric analysis⁴¹ and found to be relevant across a range of temperatures and pressures relevant to solid oxide cell operation. Our selection of fixed compositions implies a closed boundary system that does not allow exchange of oxygen with the environment once the parameter x has been selected. This necessarily implies a variable thermodynamic environment (e.g., temperature and oxygen partial pressure) to make the compositions considered stable because the actual oxygen stoichiometry is sensitive to the thermodynamic environment. For instance, for $x = 0$, SrTiO_3 is stable at pressures close to atmospheric at room temperature, whereas for $x = 1$, $\text{Sr}_2\text{Fe}_2\text{O}_5$ requires lower pressures (est. 10^{-11} atm at temperatures around 100°C ⁴²). For STF, desirable mixed ionic/electronic conducting properties and good stability are obtained for small to intermediate $x \approx 0.35$. For $x \approx 0.35$, the reference state (fully ionic compensation) is experimentally observed under typical solid oxide fuel cell operating temperatures $600\text{--}1000^\circ\text{C}$ in a wide range of pressures ranging from 10^{-18} to 10^{-3} atm.⁴¹ Thus, the reference composition selected here is practically useful for understanding properties at experimentally relevant conditions, but becomes relevant only at much lower oxygen partial pressures as x approaches 1 for the same temperature range.

2.2. Cluster Expansion and Monte Carlo Simulation. The energies of different configurations of the disordered

$\text{Sr}(\text{Ti}_{1-x}\text{Fe}_x)\text{O}_{3-x/2}$ alloy are described using a cluster expansion model. The total energy of a particular configuration is expressed as^{43,44}

$$E = \sum_{\alpha \in \text{clusters}} \left(\varepsilon_{\alpha} \prod_{i \in \alpha} s_i \right) \quad (1)$$

Here, ε_{α} denotes the coefficient (ECI, effective cluster interaction) representing the energy contribution from cluster α and s_i that are variables representing which species is present at each site. The clusters α used include monomers, dimers, trimers, and tetramers. In the $\text{Sr}(\text{Ti}_{1-x}\text{Fe}_x)\text{O}_{3-x/2}$ configuration space, the disorder appears in two main forms: on the B-site (Ti/Fe) sublattice and on the oxygen sublattice (which can contain an oxygen atom or an oxygen vacancy). As a result, the cluster expansion is built upon the Ti/Fe and O/ V_{O} sublattice only and Sr atoms are present only as “spectators” in our model. When selecting clusters, we set a cutoff distance of 8 Å for dimers and trimers and 6 Å for tetramers (details in the Supporting Information). This resulted in the following number of clusters: 1 monomer, 8 dimers, 13 trimers, and 4 tetramers. The ECI is determined by fitting across a variety of samples containing different distributions of atoms.

Rather than allowing full compositional variation,^{45–50} the cluster expansion is restricted to the reference composition $\text{Sr}(\text{Ti}_{1-x}\text{Fe}_x)\text{O}_{3-x/2+\delta}$ with fixed $\delta = 0$. This nominally allows both transition metals to maintain, on average, their most favorable oxidation state (Ti^{4+} and Fe^{3+}) as x varies between $0 < x < 1$ along a smooth transition between SrTiO_3 and $\text{Sr}_2\text{Fe}_2\text{O}_5$ and enables us to develop a cluster expansion across the full composition space spanning between two inequivalent crystal structures SrTiO_3 ($Pm\bar{3}m$) and $\text{Sr}_2\text{Fe}_2\text{O}_5$ ($I2cm$). It additionally ensures fitting of the ECI within parts of composition space more similar to those occurring in reality, rather than less realistic stoichiometries.

Once the ECI is determined, the cluster expansion is then used in Monte Carlo simulations to identify low-energy configurations and high-temperature configurations for the given supercell size.^{48,49,51,52} With these configurations, the electronic structure of $\text{Sr}(\text{Ti}_{1-x}\text{Fe}_x)\text{O}_{3-x/2}$ and its temperature dependence can be directly assessed. We use CEMC to obtain representative configurations at $T = 0$ K (low-energy configuration) and higher temperature $T = 1000$ K. These configurations are used to characterize optical and electronic properties using DFT + U . To obtain the representative structures at $T = 1000$ K, CEMC simulations are performed to generate the probability distribution of different energies and a configuration with the most likely energy is chosen for further analysis (details in the Supporting Information).

2.3. Structures Used for Comparison. To demonstrate the value of the cluster expansion for generating realistic configurations, we compare the electronic structure of the CEMC-generated structures to four hypothetical configurations: two ordered structures, SQSs, and so-called “randomly generated structures”.

The first-ordered structure is an ordered mixture in which the Fe/Ti and the O/ V_{O} sublattices each exhibit a regular order. On the B-site sublattice, Fe atoms at concentration x are introduced in an ordered manner so that they are maximally separated; on the oxygen sublattice, oxygen vacancies of concentration $x/2$ are introduced in an ordered manner so that they are maximally separated. This gives rise to configurations where V_{O} is adjacent to both Ti and Fe atoms. The second-

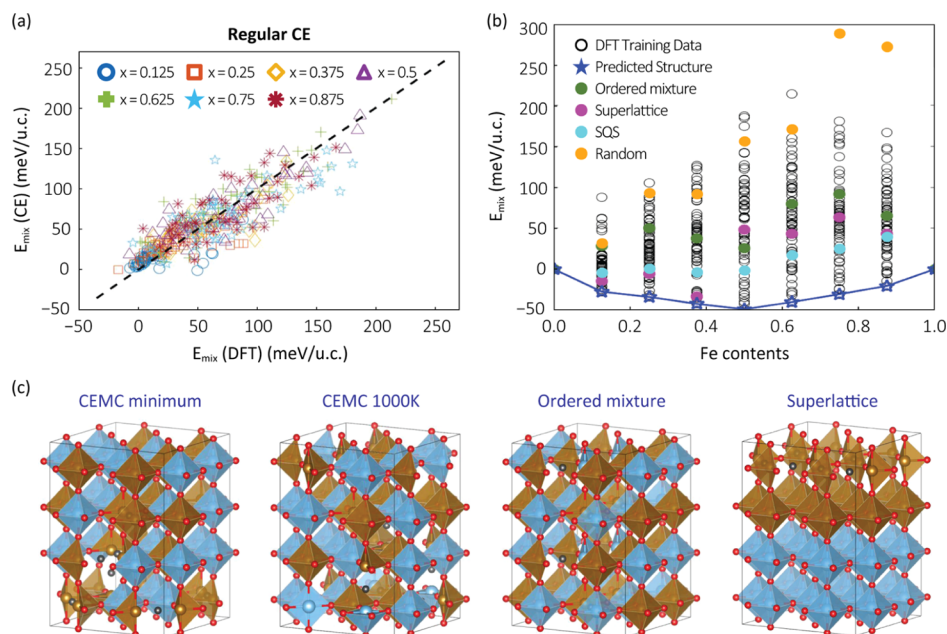


Figure 2. (a) Linear least-squares fitting of mixing energy using cluster expansion; “u.c.” denotes the five-atom unit cell of the conventional perovskite lattice. (b) Convex hull showing the lowest energy configurations predicted from Monte Carlo simulation. The training data, two ordered structures, SQSs, and random structures are shown for comparison. (c) Atomic configurations of CEMC-predicted lowest energy configurations, CEMC-predicted structure at $T = 1000$ K, and two types of ordered structures. For the convenience of visualization, A-site strontium atoms are not shown.

ordered structure is a superlattice composed of distinct local domains of SrTiO_3 and $\text{Sr}_2\text{Fe}_2\text{O}_5$. The upper part of the simulation cell is occupied by $\text{Sr}_2\text{Fe}_2\text{O}_5$ and the bottom by SrTiO_3 . The superlattice reflects the case of minimal $\text{SrTiO}_3/\text{Sr}_2\text{Fe}_2\text{O}_5$ mixing possibly for the fixed supercell size. Overall, the two hypothetical ordered structures represent extreme cases of (i) regular uniform mixing of Fe atoms in the Ti lattice and oxygen vacancies in the oxygen sublattice and (ii) the least possible degree of mixing.

We also compare the CEMC structures to SQSs and randomly generated structures. The SQS method⁵³ is used to generate chemically disordered configurations that mimic the radial correlation functions of a fully random alloy as closely as possible. For generating the SQSs for different compositions, we use a modified version^{54,55} of the ATAT package.⁵⁶ The values of the error correlation function for each composition and the different SQSs for each composition can be found in the [Supporting Information](#). The randomly generated structures are obtained by distributing the desired concentration of Fe atoms and V_{O} amongst the B-sites and oxygen sublattice, respectively, at sites selected at random.

3. RESULTS AND DISCUSSION

3.1. Cluster Expansion Training and Energy Convex Hull. The first task is to determine the ECI and the convex hull for $0 < x < 1$. We sampled the compositional space $\text{Sr}(\text{Ti}_{1-x}\text{Fe}_x)\text{O}_{3-x/2}$ at seven Fe concentrations given by $x = 0.125, 0.25, 0.375, 0.5, 0.625, 0.75,$ and 0.875 . For each, 50 random structures are generated for fitting the ECI. We then used an iterative approach in which the current ECI and $T = 0$ K Monte Carlo sampling are used to predict lowest energy configurations, and these new configurations are then analyzed in DFT and added to the training set to obtain the next set of ECI. This procedure is repeated until a self-consistent prediction of lowest energy configurations is obtained. Within

each step of the iterative procedure, 2×10^5 CEMC steps were carried out while searching for the lowest energy configuration. Because of the large number of vacancies present in STF, for some structures in the training set, during DFT geometry optimization, some oxygen atoms shifted from their initial site to a nearby vacant site. In these cases, the final sites of the atoms were used to train the cluster expansion and determine the ECI.

The ultimate resulting fit comparing DFT + U to cluster expansion energies is shown in [Figure 2a](#). A linear least-squares fitting of the 350 datasets from the DFT + U results in an overall root-mean-squared error (RMSE) of 4.33 meV/atom for the 27 cluster interaction coefficients (26 clusters and intercept). We also implemented a recently proposed Bayesian approach⁵² to determine the cluster interaction coefficients, which yielded similar results.

To establish the predictive (in addition to descriptive) capacity of the cluster expansion and ensure against overfitting, we carried out a leave-one-out cross-validation. The cross-validation score is expressed as

$$CV^2 = \frac{1}{N_{\sigma}} \sum_{\sigma} (E_{\text{mix}}^{\sigma} - \hat{E}_{\text{mix}}^{\sigma})^2 \quad (2)$$

where $\hat{E}_{\text{mix}}^{\sigma}$ is the cluster expansion (predicted) value of mixing internal energy on the test set σ using the ECI obtained from the training subset, E_{mix}^{σ} is the DFT-computed (true) value of the mixing internal energy, and N_{σ} is the total number of configurations. The cross-validation score represents how well the cluster expansion predicts energies for configurations outside of the fitting set and thus gives an indication of the predictive capability of the model. A cross-validation score of 4.76 meV/atom is obtained. Therefore, both RMSE and CV scores indicate that our model provides reasonable prediction of energetics within the configuration space.

Figure 2b shows the distribution of mixing energies across the full composition range and the convex hull constructed from the lowest energy configurations obtained. When considering Figure 2b, it is important to note that as x varies, there is an implied variation in the oxygen partial pressure as described previously. The mixing energy is given by

$$E_{\text{mix}} = E_{\text{Sr}(\text{Ti}_{1-x}\text{Fe}_x)\text{O}_3} - (1-x) \cdot E_{\text{SrTiO}_3} - x \cdot E_{\text{Sr}_2\text{Fe}_2\text{O}_5} \quad (3)$$

where $E_{\text{Sr}(\text{Ti}_{1-x}\text{Fe}_x)\text{O}_3}$, E_{SrTiO_3} , and $E_{\text{Sr}_2\text{Fe}_2\text{O}_5}$ are the calculated energy of $\text{Sr}(\text{Ti}_{1-x}\text{Fe}_x)\text{O}_3$, SrTiO_3 , and $\text{Sr}_2\text{Fe}_2\text{O}_5$, respectively. The set of lowest energy configurations across all compositions, denoted by the blue line, yields the curve for the mixing energy. The negative mixing energy across all compositions indicates that the energy of the mixture is always lower than that of the phase-separated SrTiO_3 and $\text{Sr}_2\text{Fe}_2\text{O}_5$ and that a full solid solution is possible across the full composition range, consistent with experimental observations.^{8,9}

We also show in Figure 2b the energies of the two ordered structures (the ordered mixture and the superlattice), the SQSs, and the randomly generated structures for comparison. The energies of all comparison structures lie above the convex hull. The value of the cluster expansion is evident when comparing the energies of the lowest energy structures to those of the SQSs and randomly generated structures. The use of SQSs or randomly generated structures to analyze the STF system would result in higher energy configurations that likely would exhibit different characteristics and properties than those of the cluster expansion low-energy configurations. The energy difference is particularly large for the randomly generated structures as the Fe concentration increases because of the configurational space associated with the large number of V_{O} .

Figure 2c shows a representative low-energy $T = 0$ K configuration and $T = 1000$ K configuration obtained using CEMC at the composition of $x = 0.5$ as well as the two comparison ordered structures: the ordered mixture and the superlattice. The Sr sublattice is not shown because the lattice disorder arises from Ti/Fe cation and O/ V_{O} distribution alone. Along the convex hull, we do not observe long-ranged, well-ordered structures as may typically be expected at $T = 0$ K (true ground state), likely because of the imperfect sampling of configurations or the use of a simulation cell that is not a supercell of the ground state unit cell (ordered structures have also not been reported in the experiment). The lowest energy structures found do however contain several Fe– V_{O} –Fe trimers and Fe– V_{O} dimers, which locally resemble the structure of $\text{Sr}_2\text{Fe}_2\text{O}_5$. The prevalence of Fe– V_{O} within the lowest energy structures is also reflected in the fitted ECI: the contribution to the total energy for the Fe– V_{O} (Table S1) has the largest magnitude amongst all two-body contributions (–5.7 eV), several eV larger than the next largest (O– V_{O} pair, –0.75 eV). This is consistent with the presence of short-range order in STF and results from X-ray absorption spectroscopy, indicating the presence of V_{O} in the first shell around Fe.³¹ At higher temperatures, these clusters are still present to a slightly lesser extent.^{57,58}

From Figure 2b, the energy of the two ordered structures is also always higher than the CEMC low-energy configuration. This can be understood by comparing the two sets of ordered structures with the CEMC-predicted lowest energy structure. Two observations are relevant. First, Ti and Fe cations have a

tendency to mix with each other fairly randomly. Second, as noted above, V_{O} tends to remain adjacent to Fe instead of Ti atoms and the low-energy configurations contain Fe– V_{O} –Fe structures that locally resemble $\text{Sr}_2\text{Fe}_2\text{O}_5$, largely consistent with the maintenance of Ti^{4+} and Fe^{3+} oxidation states. In experiments, Fe^{3+} is observed under a wide range of pressures and temperatures.^{8,31,57,59} In the ordered mixture, Fe atoms are introduced periodically in the B-site sublattice and V_{O} is introduced periodically into the oxygen sublattice without regard to the neighboring B-site species. This results in fewer Fe– V_{O} and oxidation states that deviate from Ti^{4+} and Fe^{3+} . On the other hand, the superlattice offers the least mixing of Ti/Fe cations. As a result, a structure as suggested by the CEMC in Figure 2c is more energetically favorable because it allows random mixing of Fe/Ti on the B-site sublattice and clustering of oxygen vacancies around Fe atoms.

3.2. Electronic Structure and Optical Properties of the $\text{Sr}(\text{Ti}_{1-x}\text{Fe}_x)\text{O}_{3-x/2}$ Alloy. We now use the CEMC configurations to assess the electronic structure of $\text{Sr}(\text{Ti}_{1-x}\text{Fe}_x)\text{O}_{3-x/2}$ across the composition space. The band gaps of the lowest energy structures at the seven selected compositions from SrTiO_3 to $\text{Sr}_2\text{Fe}_2\text{O}_5$ are calculated using DFT + U and presented in Figure 3. Results for the two ordered structures, SQSs, and randomly generated structures are also given for comparison.

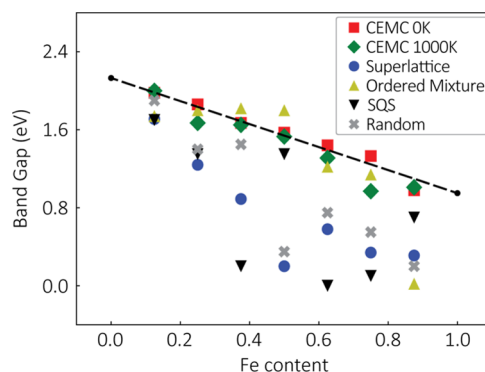


Figure 3. Evolution of band gap with Fe content. For the lowest energy and $T = 1000$ K structures, showing that the band gap smoothly decreases with increasing Fe content with little bowing evident. The band gap of the ordered structures and random structures is shown for comparison.

Figure 3 shows that there are fluctuations in the band gap as the Fe content increases for the ordered and the random structures, without any obvious systematic trends. On the other hand, for the CEMC minimum, the band gap decreases smoothly from 2.13 to 0.95 eV (DFT + U predicted gaps of SrTiO_3 and $\text{Sr}_2\text{Fe}_2\text{O}_5$). The band gap reduction with increased Fe content has been reported in previous experimental studies.^{41,57,60} Whereas many alloys (Si/Ge, e.g.⁶¹) exhibit a parabolic dependence of the band gap on the composition according to Vegard's law (linear mixing) with a bowing parameter;^{8,62–65} here, the bowing parameter is quite small, which makes the band gap evolution appear linear. This is consistent with previous experimental results by Rothschild et al.⁸ The results for the $T = 1000$ K configurations are also shown in Figure 3. Minimal differences are observed compared to the ground state structures, with these also showing a smooth decrease in band gap across the composition space. (Note that in real systems, heating to $T = 1000$ K can cause the

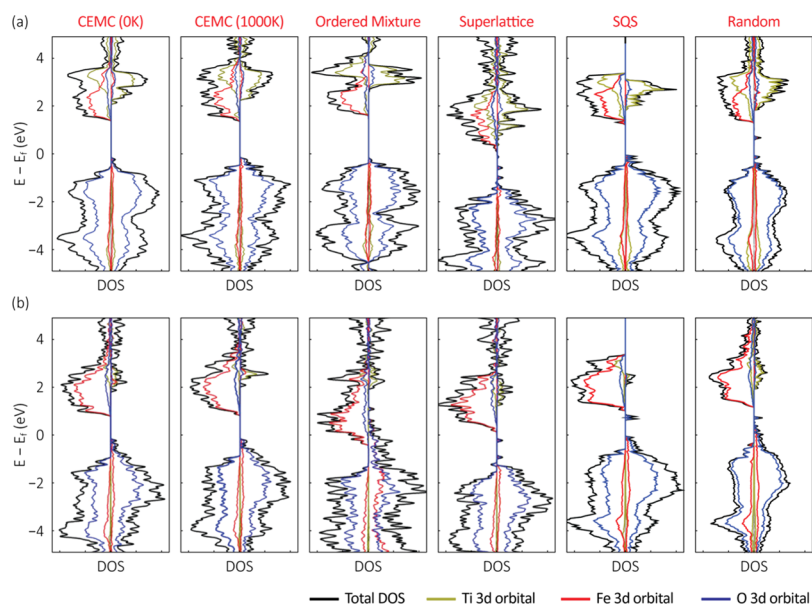


Figure 4. Site and orbital PDOS of the six configurations of $\text{Sr}(\text{Ti}_{1-x}\text{Fe}_x)\text{O}_{3-x/2}$ at (a) $x = 0.5$ and (b) $x = 0.875$.

oxygen content to deviate from $\delta = 0$, which is not accounted here. However, for small deviations, δ this is not expected to alter significantly our trends.)

In Figure 4, we consider how the specific atomic configuration affects the electronic density of states. Before considering Figure 4 in detail, it is necessary to understand how the projected density of states (PDOS) evolve with increasing Fe content in STF in the first place. As shown in our previous work,²⁶ the PDOS of STF to a large extent resemble a mixture of the PDOS of end members SrTiO_3 and $\text{Sr}_2\text{Fe}_2\text{O}_5$. SrTiO_3 is a typical band insulator, with valence bands composed of O 2p states and conduction bands composed of Ti 3d states. The PDOS of $\text{Sr}_2\text{Fe}_2\text{O}_5$ are more complex: Fe^{3+} corresponds to a high spin $3d^5$ valence, so the PDOS show a large exchange splitting between the completely filled majority and completely empty minority spin Fe 3d states. The majority spin Fe 3d states lie below the valence band maxima (VBM) edge, which is composed of O 2p states. The minority spin Fe 3d states meanwhile comprise the $\text{Sr}_2\text{Fe}_2\text{O}_5$ conduction bands. The leftmost panels in Figure 4a,b show the PDOS of the CEMC lowest energy structure at iron contents corresponding to $x = 0.5$ and $x = 0.875$, respectively. The PDOS of STF at these compositions clearly show elements of the PDOS of both end members: O 2p-derived valence bands and conduction bands that arise from hybridized Ti 3d and the empty, minority spin Fe 3d states. The band gap is smaller for $x = 0.875$ than $x = 0.5$, consistent with our results in Figure 3 and the notion of a smooth evolution of the gap across the composition space from $0 < x < 1$. For these low-energy configurations, importantly, there are little to no mid gap energy levels present. These features of the PDOS remain even for the CEMC $T = 1000$ K structures for $x = 0.5$ and $x = 0.875$ in Figure 4a,b.

It is useful next to consider how the observed trends in the PDOS are similar to or differ from those of the ordered structures, SQSs, or randomly generated structures also shown in Figure 4. First, the general features of an O 2p-derived valence band and a Ti 3d/Fe 3d-derived conduction band are preserved across all of these structures. Second, the PDOS of the CEMC structures share a stronger resemblance to those of

the SQSs and randomly generated structure than the ordered mixture and the superlattice. The closer resemblance to the SQSs and randomly generated structure results from the reduced degree of order in comparison to the two ordered structures. Even so, there are still some differences between the CEMC structures and the SQSs and randomly generated structures, however. Most notably, the PDOS for the SQSs and the randomly generated structures exhibit mid gap states that are not present in the CEMC structures. These states arise from the less favorable local atomic orderings that disrupt the smooth mixing. So long as the structures largely consist of local “patches” of SrTiO_3 and of $\text{Sr}_2\text{Fe}_2\text{O}_5$ (such as Fe–V_O–Fe chains) as in the CEMC configurations, the PDOS can be reasonably described as a mixture of the PDOS of the end member compounds. Deviations from these configurations, especially Fe atoms without neighboring V_O, meanwhile give rise to the states in the gap. The existence of such mid gap states has indeed been surmised from the experiment in the past. Depending on the configuration, they tend to be O 2p/Fe 3d hybridized states that can appear near the VBM (Fe^{4+}), at mid gap (Fe^{3+}), or toward the conduction band minima (CBM) (Fe^{2+}).

Although the differences between the PDOS of the CEMC structures and the SQSs and randomly generated structures are more subtle and can be explained from the framework of STF as a mixture of SrTiO_3 and $\text{Sr}_2\text{Fe}_2\text{O}_5$, the difference with the PDOS of the two ordered structures is (not surprisingly) more dramatic in Figure 4. Interestingly, for $x = 0.5$, the CEMC PDOS are similar to the ordered mixture, whereas for $x = 0.875$, they are more similar to the superlattice. For example, at $x = 0.5$ (Figure 4a), the superlattice exhibits a much smaller band gap, differences in the elemental contributions to the band edge states, and mid gap levels. The low-lying states of the superlattice conduction band exhibit a more mixed Ti 3d and Fe 3d orbital nature than the CEMC structures and the ordered mixture. The occupied mid gap states again mainly arise from Fe 3d orbitals near the valence band edge. On the other hand, for $x = 0.875$ (Figure 4b), the shape and magnetic features of the CEMC structures are more similar to the

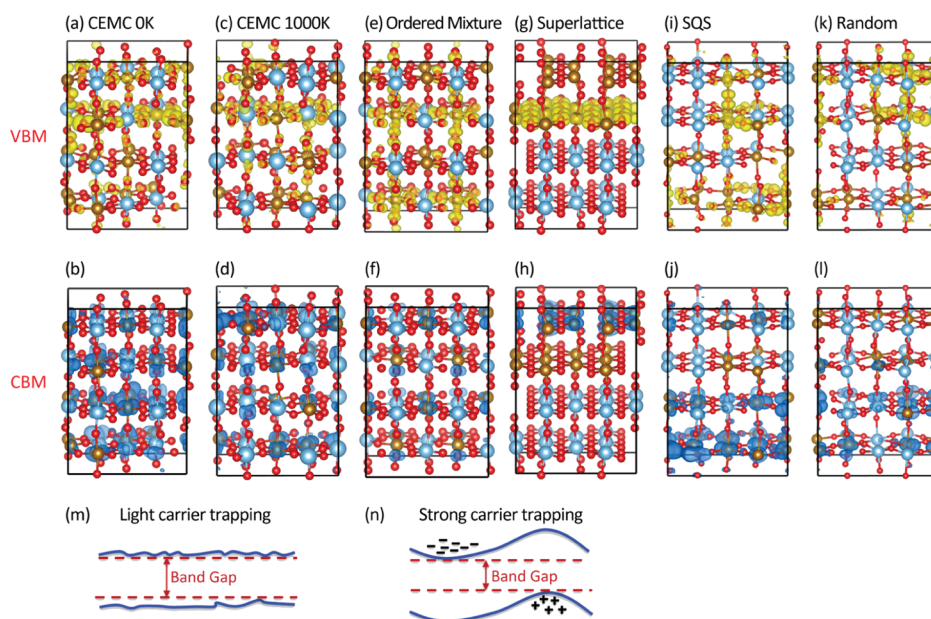


Figure 5. Charge density of the $\text{SrTi}_{0.5}\text{Fe}_{0.5}\text{O}_{2.75}$ VBM and CBM. (a,b) VBM and CBM for CEMC predicted lowest energy structure; (c,d) VBM and CBM CEMC equilibrium structure at $T = 1000$ K; (e,f) VBM and CBM for ordered mixture; (g,h) VBM and CBM for superlattice; (i,j) VBM and CBM for SQS; (k,l) VBM and CBM for randomly generated structure; (m) schematic showing light degree of carrier trapping due to delocalization of VBM and CBM; (n) schematic showing strong degree of carrier trapping due to the spatially localized band edges. Strontium atoms are not shown.

superlattice and different from the ordered mixture for which the gap has closed and the system is metallic.

To understand why the CEMC PDOS are more similar to the ordered mixture for $x = 0.5$, whereas for $x = 0.875$, they are more similar to the superlattice, we consider the effects of Ti/Fe ordering and V_O distribution. The $x = 0.5$ composition represents the largest degree of mixing between Ti and Fe atoms, so differences in the degree of Ti/Fe order/disorder dominate the nature of the density of states. The superlattice represents the case of minimal Ti and Fe mixing, causing the large observed difference in the PDOS. On the other hand, $x = 0.875$ corresponds to the largest V_O concentration considered. At this composition, the electronic structure is sensitive to the V_O distribution and correspondingly the oxidation state of each Ti/Fe atom. In the ordered mixture, V_O appears adjacent to both Ti and Fe atoms which on average shifts the oxidation states of both species more toward +3. These shifts lead to realignment of energy levels and ultimately a metallic structure.

Next in Figure 5, we explore how the Ti/Fe and oxygen vacancy distribution could affect electronic carrier transport by considering the spatial charge distribution of the valence band and conduction band edges and their degree of localization. This is shown for $x = 0.5$. High carrier mobilities beneficial for transport would be associated with delocalized band edge charge densities, whereas undesirable localized band edges may instead result in carrier trapping. These two cases are shown schematically in Figure 5m,n. Figure 5a–d show the charge density of the VBM and the CBM for the $T = 0$ K and $T = 1000$ K CEMC structures, which show similar features. As expected from the PDOS in Figure 4, the VBM states are largely O 2p derived, with some degree of Fe 3d mixed in, whereas the CBM states arise largely from the minority spin Fe 3d states. As exhibited in Figure 5a–d, both the CBM and VBM are spatially delocalized and distributed throughout the supercell. The delocalized nature is a consequence of the combined effects of the tendency for random mixing of Ti/Fe

and a tendency for V_O to be present near the Fe species. For example, the random mixing of Ti/Fe ensures that the Fe atoms are evenly distributed throughout the B-site sublattice and thus spatially spread out. Because the VBM is composed of states derived from Fe– V_O clusters, the tendency for the V_O to cluster around these distributed Fe atoms results in a spatially delocalized VBM.

By contrast, for the two ordered structures, the trends are different. For the ordered mixture, we found that the VBM mainly arises from Fe–O networks for Fe atoms coordinated with 5 oxygen atoms and is thus reasonably delocalized (Figure 5e). Consistent with the PDOS in Figure 4a, Ti atoms with a full octahedral O coordination (Figure 5f) dominate the CBM which appears patchy and disconnected. Such localized states could serve as traps for carriers, reducing mobility and transport as suggested schematically in Figure 5n. For the superlattice, the VBM and CBM are highly localized to distinct superlattice planes within the $\text{Sr}_2\text{Fe}_2\text{O}_5$ region. The VBM is dominated by Fe atoms with a full octahedral coordination at the “interface” (Figure 5g), whereas the CBM comes from Fe with tetrahedral O coordination (Figure 5h) one plane above. Moreover, the mid gap states present in the superlattice can facilitate electron–hole recombination. This reveals that the combination of Ti/Fe mixing together with a tendency for vacancy clustering around Fe atoms, when present simultaneously, offers an advantage for electronic transport not exhibited by either of the ordered structures. The SQSs and random structures are somewhat similar to the CEMC structures, although these also exhibit mid gap states that could limit transport.

Last, we show the effect of composition on the optical absorption of STF. The calculated absorption spectrum based on DFT + U is given in Figure 6. Here, the CEMC ground state structures are used to obtain the dielectric matrix.⁶⁶ The absorption coefficient is formulated from the complex dielectric function as

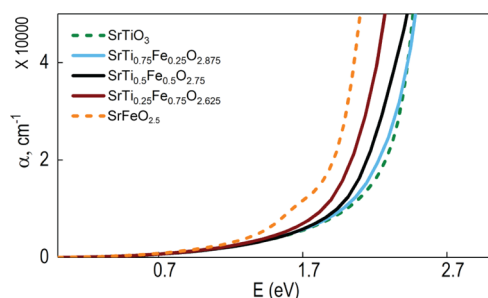


Figure 6. Optical absorption for selected compositions of Sr($\text{Ti}_{1-x}\text{Fe}_x$) $\text{O}_{3-x/2}$ alloy for the lowest energy configurations.

$$\alpha(\omega) = \frac{\sqrt{2}\omega}{c} \{[\varepsilon_1^2(\omega) + \varepsilon_2^2(\omega)]^{1/2} - \varepsilon_1(\omega)\}^{1/2} \quad (4)$$

where $\varepsilon^{(1)}(\omega)$ and $\varepsilon^{(2)}(\omega)$ refer to the real and imaginary parts of dielectric function, respectively, and c is the speed of light. From Figure 6, absorption becomes gradually enhanced with increasing Fe content as reported in previous studies.^{8,59} The monotonic variation is consistent with the band gap evolution shown in Figure 3. Note that the optical absorption spectrum depends on both the band gap and the density of states at the conduction and valence band extrema and the transition oscillator strengths. Correspondingly, the optical absorption may not vary perfectly uniform with the composition, which likely accounts for the similar absorption coefficients observed for SrTiO₃ and SrTi_{0.75}Fe_{0.25}O_{2.875}.

4. CONCLUSIONS

To conclude, we present a computational framework to consider the effects of composition and order/disorder in the STF solid solution, a MIEC. Using cluster expansion modeling and Monte Carlo simulations, energetics and realistic configurations of the Sr($\text{Ti}_{1-x}\text{Fe}_x$) $\text{O}_{3-x/2}$ can be predicted across the full composition space spanning from SrTiO₃ to Sr₂Fe₂O₅. We use the framework to generate representative configurations and assess their properties using DFT. The analysis reveals the connection between Ti/Fe cation disorder and oxygen vacancy distribution on the electronic structure. Several predicted trends are in agreement with prior experimental results including evolution of the band gap and optical absorption with Fe content and the tendency for short-ranged ordering to be present. It is found that Ti/Fe cation disorder together with oxygen vacancy clustering around Fe atoms gives rise to spatially delocalized band edge states, which may facilitate carrier transport in the lattice. The properties of the CEMC-derived structures in some instances are different from those of SQSs and comparison ordered structures, highlighting the value of CEMC for obtaining a more realistic understanding of the properties of the complex, nondilute material system. This work not only provides mechanistic understanding of the disorder and electronic structure of Sr($\text{Ti}_{1-x}\text{Fe}_x$) $\text{O}_{3-x/2}$ but also suggests a computational strategy for analysis of complex perovskite solutions in fuel and electrolysis cells and other applications using perovskite-derivative compounds exhibiting lattice disorder. The approach presented here may also be extended for the prediction of ionic transport coefficients using realistic configuration ensembles generated from CEMC.

■ ASSOCIATED CONTENT

Supporting Information

The Supporting Information is available free of charge on the ACS Publications website at DOI: 10.1021/acs.chemmater.8b04285.

Cluster expansion description and ECIs, Monte Carlo sampled configurations, and SQS configurations (PDF)

■ AUTHOR INFORMATION

Corresponding Author

*E-mail: ertekin@illinois.edu.

ORCID

Namhoon Kim: 0000-0002-2177-5281

Nicola H. Perry: 0000-0002-7207-2113

Elif Ertekin: 0000-0002-7816-1803

Notes

The authors declare no competing financial interest.

■ ACKNOWLEDGMENTS

B.O., T.C., N.K., N.H.P., N.R.A., and E.E. gratefully acknowledge the support of the NSF and JSPS under the JSPS-NSF Partnerships for International Research and Education (PIRE), U.S. NSF grant no. 1545907. N.H.P. and E.E. further acknowledge the support of the International Institute for Carbon Neutral Energy Research (WPI-I2CNER), sponsored by the Japanese Ministry of Education, Culture, Sports, Science, and Technology. T.M. acknowledges support from ONR N00014-15-1-2494. This research is part of the Blue Waters sustained-petascale computing project, which is supported by the National Science Foundation (awards OCI-0725070 and ACI-1238993) and the state of Illinois. Blue Waters is a joint effort of the University of Illinois at Urbana-Champaign and its National Center for Supercomputing Applications.

■ REFERENCES

- (1) Adler, S. B. Factors Governing Oxygen Reduction in Solid Oxide Fuel Cell Cathodes†. *Chem. Rev.* **2004**, *104*, 4791–4844.
- (2) Jacobson, A. J. Materials for Solid Oxide Fuel Cells†. *Chem. Mater.* **2010**, *22*, 660–674.
- (3) Wang, K.; Hissel, D.; Péra, M. C.; Steiner, N.; Marra, D.; Sorrentino, M.; Pianese, C.; Monteverde, M.; Cardone, P.; Saarinen, J. A Review on solid oxide fuel cell models. *Int. J. Hydrogen Energy* **2011**, *36*, 7212–7228.
- (4) Muñoz-García, A. B.; Pavone, M.; Ritzmann, A. M.; Carter, E. A. Oxide ion transport in Sr₂Fe_{1.5}Mo_{0.5}O_{6-δ}, a mixed ion-electron conductor: new insights from first principles modeling. *Phys. Chem. Chem. Phys.* **2013**, *15*, 6250–6310.
- (5) Mahato, N.; Banerjee, A.; Gupta, A.; Omar, S.; Balani, K. Progress in material selection for solid oxide fuel cell technology: A review. *Prog. Mater. Sci.* **2015**, *72*, 141–337.
- (6) Suntivich, J.; May, K. J.; Gasteiger, H. A.; Goodenough, J. B.; Shao-Horn, Y. A Perovskite Oxide Optimized for Oxygen Evolution Catalysis from Molecular Orbital Principles. *Science* **2011**, *334*, 1383–1385.
- (7) Muñoz-García, A. B.; Ritzmann, A. M.; Pavone, M.; Keith, J. A.; Carter, E. A. Oxygen Transport in Perovskite-Type Solid Oxide Fuel Cell Materials: Insights from Quantum Mechanics. *Acc. Chem. Res.* **2014**, *47*, 3340–3348.
- (8) Rothschild, A.; Menesklou, W.; Tuller, H. L.; Ivers-Tiffée, E. Electronic Structure, Defect Chemistry, and Transport Properties of SrTi_{1-x}Fe_xO_{3-y} Solid Solutions. *Chem. Mater.* **2006**, *18*, 3651–3659.
- (9) Metlenko, V.; Jung, W.; Bishop, S. R.; Tuller, H. L.; De Souza, R. A. Oxygen diffusion and surface exchange in the mixed conducting

oxides $\text{SrTi}_{1-y}\text{Fe}_y\text{O}_{3-\delta}$. *Phys. Chem. Chem. Phys.* **2016**, *18*, 29495–29505.

(10) Gryaznov, D.; Merkle, R.; Kotomin, E. A.; Maier, J. Ab initio modelling of oxygen vacancies and protonic defects in $\text{La}_{1-x}\text{Sr}_x\text{FeO}_{3-\delta}$ perovskite solid solutions. *J. Mater. Chem. A* **2016**, *4*, 13093–13104.

(11) Heifets, E.; Kotomin, E. A.; Bagaturyants, A. A.; Maier, J. Thermodynamic stability of stoichiometric LaFeO_3 and BiFeO_3 : a hybrid DFT study. *Phys. Chem. Chem. Phys.* **2017**, *19*, 3738–3755.

(12) Choi, Y.; Lin, M. C.; Liu, M. Computational Study on the Catalytic Mechanism of Oxygen Reduction on $\text{La}_{0.5}\text{Sr}_{0.5}\text{MnO}_3$ in Solid Oxide Fuel Cells. *Angew. Chem., Int. Ed.* **2007**, *46*, 7214–7219.

(13) Ong, K. P.; Fan, X.; Subedi, A.; Sullivan, M. B.; Singh, D. J. Transparent conducting properties of SrSnO_3 and ZnSnO_3 . *APL Mater.* **2015**, *3*, 062505.

(14) Baba, E.; Kan, D.; Yamada, Y.; Haruta, M.; Kurata, H.; Kanemitsu, Y.; Shimakawa, Y. Optical and transport properties of transparent conducting La-doped SrSnO_3 thin films. *J. Phys. D: Appl. Phys.* **2015**, *48*, 455106.

(15) Rodríguez, J.; González-Calbet, J. M. Rhombohedral $\text{Sr}_2\text{Co}_2\text{O}_5$: A new $\text{A}_2\text{M}_2\text{O}_5$ Phase. *Mater. Res. Bull.* **1986**, *21*, 429–439.

(16) Sanchez, J. M.; Ducastelle, F.; Grati, D. Generalized cluster description of multicomponent systems. *Phys. A* **1984**, *128*, 334–350.

(17) Koehl, A.; Kajewski, D.; Kubacki, J.; Lenser, C.; Dittmann, R.; Meuffels, P.; Szot, K.; Waser, R.; Szade, J. Detection of Fe^{2+} valence states in Fe doped SrTiO_3 epitaxial thin films grown by pulsed laser deposition. *Phys. Chem. Chem. Phys.* **2013**, *15*, 8311–8317.

(18) Fagg, D. P.; Kharton, V. V.; Kovalevsky, A. V.; Viskup, A. P.; Naumovich, E. N.; Frade, J. R. The stability and mixed conductivity in La and Fe doped SrTiO_3 in the search for potential SOFC anode materials. *J. Eur. Ceram. Soc.* **2001**, *21*, 1831–1835.

(19) Baker, J. N.; Bowes, P. C.; Long, D. M.; Moballegh, A.; Harris, J. S.; Dickey, E. C.; Irving, D. L. Defect mechanisms of coloration in Fe-doped SrTiO_3 from first principles. *Appl. Phys. Lett.* **2017**, *110*, 122903–122906.

(20) Kumar, A. S.; Suresh, P.; Kumar, M. M.; Srikanth, H.; Post, M. L.; Sahner, K.; Moos, R.; Srinath, S. Magnetic and ferroelectric properties of Fe doped $\text{SrTiO}_{3-\delta}$ films. *J. Phys. Conf. Ser.* **2010**, *200*, 092010.

(21) Fuentes, S.; Muñoz, P.; Barraza, N.; Chávez-Ángel, E.; Sotomayor Torres, C. M. Structural characterisation of slightly Fe-doped SrTiO_3 grown via a sol-gel hydrothermal synthesis. *J. Sol-Gel Sci. Technol.* **2015**, *75*, 593–601.

(22) van Benthem, K.; Elsässer, C.; French, R. H. Bulk electronic structure of SrTiO_3 : Experiment and theory. *J. Appl. Phys.* **2001**, *90*, 6156–6164.

(23) Ohly, C.; Hoffmann-Eifert, S.; Guo, X.; Schubert, J.; Waser, R. Electrical Conductivity of Epitaxial SrTiO_3 Thin Films as a Function of Oxygen Partial Pressure and Temperature. *J. Am. Ceram. Soc.* **2006**, *89*, 2845–2852.

(24) D'Hondt, H.; Abakumov, A. M.; Hadermann, J.; Kalyuzhnaya, A. S.; Rozova, M. G.; Antipov, E. V.; Van Tendeloo, G. Tetrahedral Chain Order in the $\text{Sr}_2\text{Fe}_2\text{O}_5$ Brownmillerite. *Chem. Mater.* **2008**, *20*, 7188–7194.

(25) Young, J.; Rondinelli, J. M. Crystal structure and electronic properties of bulk and thin film brownmillerite oxides. *Phys. Rev. B: Condens. Matter Mater. Phys.* **2015**, *92*, 174111–174210.

(26) Kim, N.; Perry, N. H.; Ertekin, E. Atomic Modeling and Electronic Structure of Mixed Ionic-Electronic Conductor $\text{SrTi}_{1-x}\text{Fe}_x\text{O}_{3-x/2+\delta}$ Considered as a Mixture of SrTiO_3 and $\text{Sr}_2\text{Fe}_2\text{O}_5$. *Chem. Mater.* **2019**, *31*, 233–243.

(27) Steinsvik, S.; Bugge, R.; Gjønnes, J.; Taftø, J.; Norby, T. The Defect Structure of $\text{SrTi}_{1-x}\text{Fe}_x\text{O}_{3-y}$ ($x = 0-0.8$) Investigated by Electrical Conductivity Measurements and Electron Energy Loss Spectroscopy (EELS). *J. Phys. Chem. Solids* **1997**, *58*, 969–976.

(28) Jung, W.; Tuller, H. L. A New Model Describing Solid Oxide Fuel Cell Cathode Kinetics: Model Thin Film $\text{SrTi}_{1-x}\text{Fe}_x\text{O}_{3-\delta}$ Mixed Conducting Oxides—a Case Study. *Adv. Energy Mater.* **2011**, *1*, 1184–1191.

(29) Perry, N. H.; Kim, J. J.; Bishop, S. R.; Tuller, H. L. Strongly coupled thermal and chemical expansion in the perovskite oxide system $\text{Sr}(\text{Ti},\text{Fe})\text{O}_3-\alpha$. *J. Mater. Chem. A* **2015**, *3*, 3602–3611.

(30) dos Santos-Gómez, L.; Porras-Vázquez, J. M.; Losilla, E. R.; Marrero-López, D. Ti-doped SrFeO_3 nanostructured electrodes for symmetric solid oxide fuel cells. *RSC Adv.* **2015**, *5*, 107889–107895.

(31) Vračar, M.; Kuzmin, A.; Merkle, R.; Purans, J.; Kotomin, E. A.; Maier, J.; Mathon, O. Jahn-Teller distortion around Fe^{4+} in $\text{Sr}(\text{Fe},\text{Ti})_{1-x}\text{O}_3-\delta$ from x-ray absorption spectroscopy, x-ray diffraction, and vibrational spectroscopy. *Phys. Rev. B: Condens. Matter Mater. Phys.* **2007**, *76*, 174107.

(32) Hohenberg, P.; Kohn, W. Inhomogeneous electron gas. *Phys. Rev. B: Solid State* **1964**, *136*, B864.

(33) Kohn, W.; Sham, L. J. Self-Consistent Equations Including Exchange and Correlation Effects. *Phys. Rev. B: Solid State* **1965**, *140*, A1133–A1138.

(34) Kresse, G.; Furthmüller, J. Efficiency of ab-initio total energy calculations for metals and semiconductors using a plane-wave basis set. *Comput. Mater. Sci.* **1996**, *6*, 15–50.

(35) Kresse, G.; Furthmüller, J. Efficient iterative schemes for ab initio total-energy calculations using a plane-wave basis set. *Phys. Rev. B: Condens. Matter Mater. Phys.* **1996**, *54*, 11169.

(36) Kresse, G.; Joubert, D. From ultrasoft pseudopotentials to the projector augmented-wave method. *Phys. Rev. B: Condens. Matter Mater. Phys.* **1999**, *59*, 1758.

(37) Perdew, J. P.; Burke, K.; Ernzerhof, M. Generalized Gradient Approximation Made Simple. *Phys. Rev. Lett.* **1996**, *77*, 3865–3868.

(38) Blöchl, P. E. Projector augmented-wave method. *Phys. Rev. B: Condens. Matter Mater. Phys.* **1994**, *50*, 17953.

(39) Loetzsch, R.; Lübcke, A.; Uschmann, I.; Förster, E.; Große, V.; Thuerk, M.; Koettig, T.; Schmidl, F.; Seidel, P. The cubic to tetragonal phase transition in SrTiO_3 single crystals near its surface under internal and external strains. *Appl. Phys. Lett.* **2010**, *96*, 071901.

(40) Auckett, J. E.; Studer, A. J.; Sharma, N.; Ling, C. D. Floating-zone growth of brownmillerite $\text{Sr}_2\text{Fe}_2\text{O}_5$ and the observation of a chain-ordered superstructure by single-crystal neutron diffraction. *Solid State Ionics* **2012**, *225*, 432–436.

(41) Kuhn, M.; Kim, J. J.; Bishop, S. R.; Tuller, H. L. Oxygen Nonstoichiometry and Defect Chemistry of Perovskite-Structured $\text{Ba}_{x}\text{Sr}_{1-x}\text{Ti}_{1-y}\text{Fe}_y\text{O}_{3-y/2+\delta}$ Solid Solutions. *Chem. Mater.* **2013**, *25*, 2970–2975.

(42) Das, T.; Nicholas, J. D.; Qi, Y. Long-range charge transfer and oxygen vacancy interactions in strontium ferrite. *J. Mater. Chem. A* **2017**, *5*, 4493–4506.

(43) Laks, D. B.; Ferreira, L. G.; Froyen, S.; Zunger, A. Efficient cluster expansion for substitutional systems. *Phys. Rev. B: Condens. Matter Mater. Phys.* **1992**, *46*, 12587.

(44) Ferreira, L. G.; Wei, S.-H.; Zunger, A. First-principles calculation of alloy phase diagrams: The renormalized-interaction approach. *Phys. Rev. B: Condens. Matter Mater. Phys.* **1989**, *40*, 3197.

(45) Thomas, J. C.; Ven, A. V. D. Finite-temperature properties of strongly anharmonic and mechanically unstable crystal phases from first principles. *Phys. Rev. B: Condens. Matter Mater. Phys.* **2013**, *88*, 214111–214113.

(46) Puchala, B.; Van der Ven, A. Thermodynamics of the Zr-O system from first-principles calculations. *Phys. Rev. B: Condens. Matter Mater. Phys.* **2013**, *88*, 094108.

(47) Van der Ven, A.; Thomas, J. C.; Xu, Q.; Bhattacharya, J. Linking the electronic structure of solids to their thermodynamic and kinetic properties. *Math. Comput. Simulat.* **2010**, *80*, 1393–1410.

(48) van de Walle, A. Multicomponent multisublattice alloys, nonconfigurational entropy and other additions to the Alloy Theoretic Automated Toolkit. *Calphad* **2009**, *33*, 266–278.

(49) Seko, A.; Yuge, K.; Oba, F.; Kuwabara, A.; Tanaka, I. Prediction of ground-state structures and order-disorder phase transitions in II-III spinel oxides: A combined cluster-expansion method and first-principles study. *Phys. Rev. B: Condens. Matter Mater. Phys.* **2006**, *73*, 184117.

(50) Seko, A.; Togo, A.; Oba, F.; Tanaka, I. Structure and Stability of a Homologous Series of Tin Oxides. *Phys. Rev. Lett.* **2008**, *100*, 045702.

(51) Ouyang, B.; Qi, W.; Liu, C.; Wang, X.; Wei, L.; Sun, C. Q. Size and shape dependent order-disorder phase transition of Co-Pt nanowires. *Comput. Mater. Sci.* **2012**, *63*, 286–291.

(52) Mueller, T. Ab initio determination of structure-property relationships in alloy nanoparticles. *Phys. Rev. B: Condens. Matter Mater. Phys.* **2012**, *86*, 144201–144205.

(53) Zunger, A.; Wei, S.-H.; Ferreira, L. G.; Bernard, J. E. Special quasirandom structures. *Phys. Rev. Lett.* **1990**, *65*, 353.

(54) von Pezold, J.; Dick, A.; Friák, M.; Neugebauer, J. Generation and performance of special quasirandom structures for studying the elastic properties of random alloys: Application to Al-Ti. *Phys. Rev. B: Condens. Matter Mater. Phys.* **2010**, *81*, 094203.

(55) Koßmann, J.; Hammerschmidt, T.; Maisel, S.; Müller, S.; Drautz, R. Solubility and ordering of Ti, Ta, Mo and W on the Al sublattice in $\text{Li}_2\text{-Co}_3\text{Al}$. *Intermetallics* **2015**, *64*, 44–50.

(56) van de Walle, A.; Asta, M.; Ceder, G. The Alloy Theoretic Automated Toolkit: A User Guide. *Calphad* **2002**, *26*, 539–553.

(57) da Silva, L. F.; M'Peko, J.-C.; Andrés, J.; Beltrán, A.; Gracia, L.; Bernardi, M. I. B.; Mesquita, A.; Antonelli, E.; Moreira, M. L.; Mastelaro, V. R. Insight into the Effects of Fe Addition on the Local Structure and Electronic Properties of SrTiO_3 . *J. Phys. Chem. C* **2014**, *118*, 4930–4940.

(58) Blokhin, E.; Kotomin, E.; Kuzmin, A.; Purans, J.; Evarestov, R.; Maier, J. Theoretical modeling of the complexes of iron impurities and oxygen vacancies in SrTiO_3 . *Appl. Phys. Lett.* **2013**, *102*, 112913.

(59) Goto, T.; Kim, D. H.; Sun, X.; Onbasli, M. C.; Florez, J. M.; Ong, S. P.; Vargas, P.; Ackland, K.; Stamenov, P.; Aimon, N. M.; et al. Magnetism and Faraday Rotation in Oxygen-Deficient Polycrystalline and Single-Crystal Iron-Substituted Strontium Titanate. *Phys. Rev. Appl.* **2017**, *7*, 024006.

(60) Mourão, H. A. J. L.; Lopes, O. F.; Avansi, W.; Pires, M. J. M.; Souza, S.; Ribeiro, C.; Mastelaro, V. R. $\text{SrTi}_{1-\gamma}\text{Fe}_\gamma\text{O}_3$ samples obtained by hydrothermal method: The effect of the amount of Fe on structural and photocatalytic properties. *Mater. Sci. Semicond. Process.* **2017**, *68*, 140–146.

(61) Weber, J.; Alonso, M. I. Near-band-gap photoluminescence of Si-Ge alloys. *Phys. Rev. B: Condens. Matter Mater. Phys.* **1989**, *40*, 5683.

(62) Donati, G. P.; Kaspi, R.; Malloy, K. J. Interpolating semiconductor alloy parameters: Application to quaternary III-V band gaps. *J. Appl. Phys.* **2003**, *94*, 5814–5819.

(63) Kuo, Y.-K.; Lin, W.-W.; Lin, J. Band-Gap Bowing Parameter of the $\text{In}_x\text{Ga}_{1-x}\text{N}$ Derived From Theoretical Simulation. *Jpn. J. Appl. Phys.* **2001**, *40*, 3157–3158.

(64) Mourad, D.; Czycholl, G.; Kruse, C.; Klembt, S.; Retzlaff, R.; Hommel, D.; Gartner, M.; Anastasescu, M. Band gap bowing of binary alloys: Experimental results compared to theoretical tight-binding supercell calculations for $\text{Cd}_x\text{Zn}_{1-x}\text{Se}$. *Phys. Rev. B: Condens. Matter Mater. Phys.* **2010**, *82*, 165204–165207.

(65) Moses, P. G.; Van de Walle, C. G. Band bowing and band alignment in InGaN alloys. *Appl. Phys. Lett.* **2010**, *96*, 021908.

(66) Gajdoš, M.; Hummer, K.; Kresse, G.; Furthmüller, J.; Bechstedt, F. Linear optical properties in the projector-augmented wave methodology. *Phys. Rev. B: Condens. Matter Mater. Phys.* **2006**, *73*, 045112.